Whole-ExM: Expansion microscopy imaging of all anatomical structures of whole larval zebrafish

Jueun Sim[1,18], Chan E Park[1,18], In Cho[1,18], Kyeongbae Min[2], Jeong-Soo Lee[3,4,5], Yosep Chong[6], Jeewon Kim[7], Jeong Seuk Kang[8], Kiryl D. Piatkevich[9,10,11], Erica E. Jung[12], Seok-Kyu Kwon[13,14], Young-Gyu Yoon[7], Edward S. Boyden[15,16,17], and Jae-Byum Chang[1*]

[1]Department of Materials Science and Engineering, Korea Advanced Institute of Science and Technology, Daejeon, Republic of Korea

[2]Department of Biomedical Engineering, Sungkyunkwan University, Suwon, Republic of Korea

[3]Disease Target Structure Research Center, Korea Research Institute of Bioscience and Biotechnology, Daejeon, Republic of Korea

[4]KRIBB School, University of Science and Technology, Daejeon, Republic of Korea

[5]Convergence Research Center for Dementia, Korea Institute of Science and Technology, Seoul, Republic of Korea

[6]Department of Hospital Pathology, Uijeongbu St. Mary's Hospital, College of Medicine, The Catholic University of Korea, Uijeongbu, Republic of Korea

[7]School of Electrical Engineering, Korea Advanced Institute of Science and Technology, Daejeon, Republic of Korea

[8]John A. Paulson School of Engineering and Applied Sciences Harvard University, Cambridge, MA, USA

[9]School of Life Sciences, Westlake University, Hangzhou, Zhejiang, China

[10]Westlake Laboratory of Life Sciences and Biomedicine, Westlake University, Hangzhou, Zhejiang, China

[11]Institute of Basic Medical Sciences, Westlake Institute for Advanced Study, Hangzhou, Zhejiang, China

[12]Department of Mechanical and Industrial Engineering, The University of Illinois at Chicago, Chicago, IL, USA

[13]Center for Functional Connectomics, Brain Science Institute, Korea Institute of Science and Technology, Seoul, Republic of Korea

[14]Division of Bio-Medical Science and Technology, KIST School, Korea University of Science and Technology, Seoul, Republic of Korea

[15]Howard Hughes Medical Institute, Cambridge, MA, USA.

[16]McGovern Institute, Massachusetts Institute of Technology, Cambridge, MA, USA.

[17]Departments of Brain and Cognitive Sciences, Media Arts and Sciences, and Biological Engineering,

Massachusetts Institute of Technology, Cambridge, MA, USA.

[18]These authors contributed equally: Jueun Sim, Chan E Park, and In Cho

*Corresponding Author: jbchang03@kaist.ac.kr

ABSTRACT

Nanoscale imaging of all anatomical structures over whole vertebrates is needed for a systematic understanding of human diseases, but this has not yet been achieved. Here, we demonstrate whole-ExM, which enables nanoscale imaging of all anatomical structures of whole zebrafish larvae by labeling the proteins of the larvae with fluorophores and expanding them four-fold. We first optimize the fluorophore selection and labeling procedure to visualize a broader range of anatomical structures. We then develop an expansion protocol for zebrafish larvae having calcified body parts. Through this process, we visualize the nanoscale details of diverse larvae organs, which have corresponding organ counterparts in humans, over the intact larvae. We show that whole-ExM retains the fluorescence signals of fluorescent proteins, and its resolution is high enough to visualize various structures that can be imaged only with electron microscopy. Whole-ExM would enable the nanoscale study of the molecular mechanisms of human diseases.

INTRODUCTION

A systematic understanding of biological systems requires an unbiased investigation of the whole organism at sub-cellular resolutions[1]. In developmental biology, for instance, a high spatial resolution is essential for discerning differences in subcellular structures or morphological details during different developmental stages, whereas full spatial coverage is needed for the quantitative analysis of organ morphogenesis from a systematic persepective[2]. Various imaging techniques have been developed to visualize whole organism, including tissue clearing[3–5], computed tomography[6], and electron microscopy[7]. Computed tomography and tissue clearing do not rely on physical sectioning and this allow for non-invasive, three-dimensional histological analysis[6,8]. Nonetheless, these approaches do not provide sub-cellular resolution beyond millimeter-scales with a sufficiently high contrast to distinguish sub-cellular structures[6]. Electron microscopy has been combined with automated sectioning to facilitate volumetric tissue imaging at a nanoscale resolution[9,10]; however, sample preparation and image reconstruction require specialized instruments and skilled personnel for the imaging of a whole organism[11]. Simple and straightforward approaches for imaging intact organisms at a subcellular resolution remain an unmet need in biology.

Expansion microscopy (ExM) combined with the labeling of functional groups of specimens with fluorophores would be an attractive candidate for satisfying such a need[12–16]. ExM can image proteins or mRNA in diverse specimens with a lateral resolution of 60-nm by physically expanding the specimens[17–23]. Recently developed ExM techniques utilizing fluorophore labeling have enabled the unbiased visualization of nanoscale details of subcellular structures and organelles by labeling various types of molecules, such as proteins[12,14,24], nucleic acids[12,16], or lipids[15,16], without antibodies[12–14,16]. However, the application of ExM to whole organisms has been limited to relatively small and simple organisms, such as bacteria[25–27], fungi[28], and parasitic micro-organisms[29]. Recently, whole-organism ExM imaging of *C. elegans* has been demonstrated[14,30]. However, ExM imaging of whole vertebrates, which share a high degree of genetic and anatomical similarities with humans, has not yet been demonstrated because of the difficulty of expanding hard body parts, such as bones.

In this paper, we demonstrate a new ExM technique, whole-ExM, which can visualize all anatomically relevant structures of whole larval zebrafish. We first show that the range of structures visualized by fluorophore *N*-Hydroxysuccinimide (NHS)-ester staining depends on the hydrophobicity of the fluorophores used. Thus, we use multiple fluorophore NHS esters with different hydrophobicities to reveal all major anatomically relevant cellular structures and cellular organelles that could not be observed with only one fluorophore NHS ester. Then, we show that even more diverse structures can be visualized when fluorophore NHS esters are applied in the middle of the digestion process compared with when they are applied before or after digestion. Finally, we optimize the ExM protocol for vertebrates in which bones and soft tissues are entangled. By combining these three approaches, we visualize all anatomically relevant structures of whole larval zebrafish with a lateral resolution of 60-nm without the need for any antibodies or a thin-slicing process (see **Supplementary Video 1** for the whole-ExM imaging of a zebrafish larva).

RESULTS

Effect of the physicochemical properties of fluorophores on the range of labeled structures

We first investigated whether all anatomically relevant structures could be visualized using fluorophore NHS-ester staining. Recently developed expansion microscopy techniques visualize diverse cellular structures and cellular organelles by conjugating fluorophores to functional groups of specific molecular types[12–14,16], such as the conjugation of fluorophore NHS esters to the primary amines of proteins[12–14]. However, the effect of fluorophores on the range of structures that can be visualized has not been studied. We hypothesized that the protein structures labeled with fluorophore NHS esters would depend on the physicochemical properties of the fluorophores, especially their hydrophobicity. To verify this hypothesis, mouse brain slices were first permeabilized with Triton X-100 and treated with 6-((acryloyl)amino)hexanoic acid (AcX), which introduces gel-anchoring moieties to proteins. The slices were then embedded in a swellable hydrogel and digested with proteinase K. Subsequently, the slices were labeled with one of seven fluorophore NHS esters with different hydrophobicities and expanded (**Supplementary Fig. 1**). Cy3, the most hydrophobic fluorophore among these seven fluorophore, showed weak staining in the nuclei but strong staining in the nuclear membranes. In addition, Cy3 NHS ester showed globular and linear structures in the cytoplasm, which corresponded to mitochondria and endoplasmic reticulum (ER), respectively (**Fig. 1a**). The signal-to-noise ratio of the labeled mitochondria and ER was sufficiently high to clearly visualize their three-dimensional structures, as shown in **Supplementary Video 2**. Another hydrophobic fluorophore NHS ester, ATTO 647N NHS ester, showed a similar staining pattern, as shown in **Fig. 1b** (see **Supplementary Fig. 2a–c** for the magnified images). We confirmed that mitochondria in the cytoplasm—and even those in neurites—were labeled with hydrophobic fluorophore NHS esters using a transgenic mouse line expressing mitochondria-targeted mScarlet (fluorescent protein) (**Supplementary Fig. 2d–f**, see **Supplementary Video 3** for a z-stack image). The hydrophobic fluorophore NHS esters strongly labeled the myelinated regions of neurons and blood vessels (**Supplementary Fig. 2g–i**).

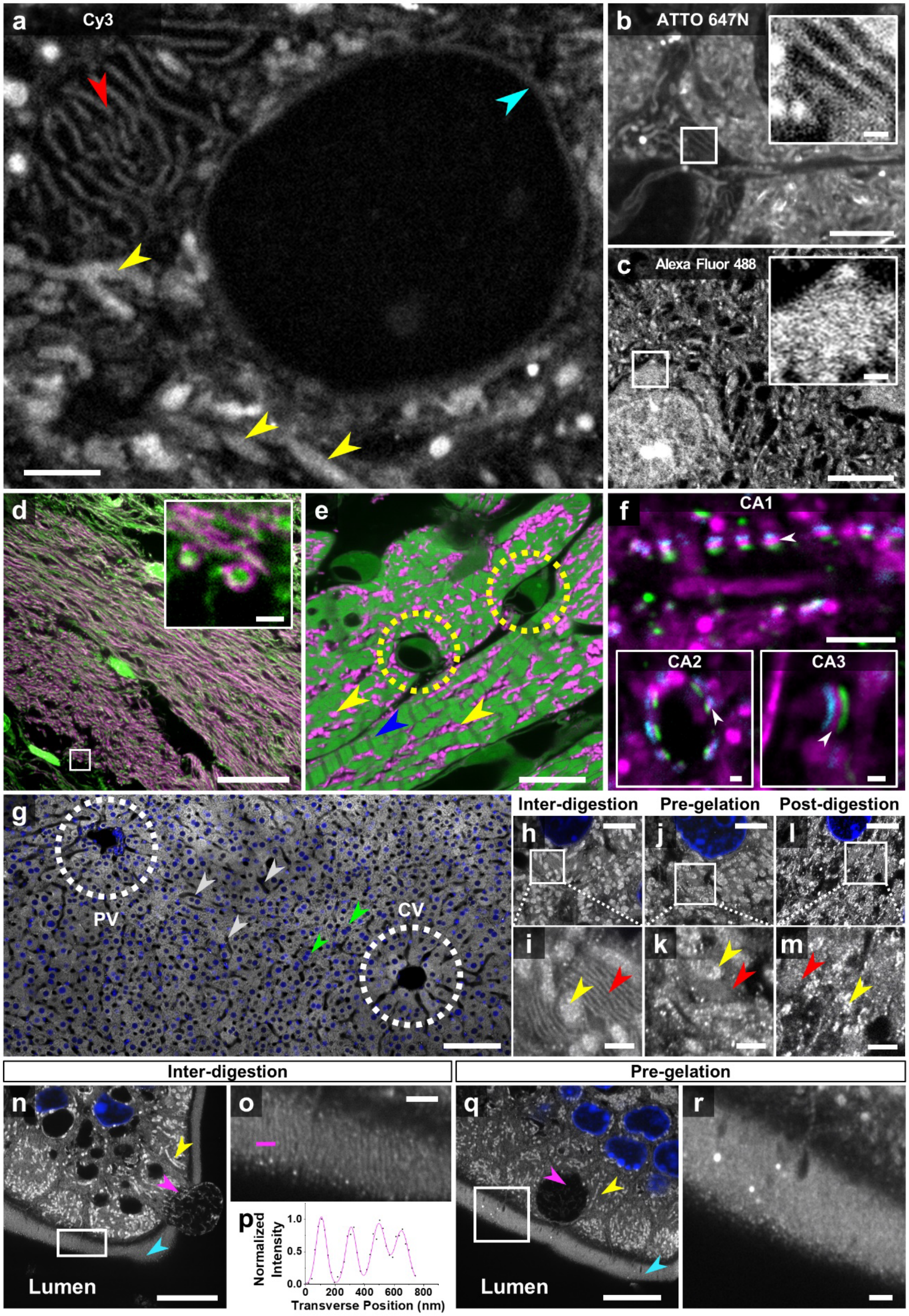
a
Cy3
b
ATTO 647N
c
Alexa Fluor 488
d
e
f
CA1
CA2
CA3
g
PV
CV
Inter-digestion
Pre-gelation
Post-digestion
h
j
l
i
k
m
Inter-digestion
Pre-gelation
n
Lumen
o
p
Normalized Intensity
1.0
0.5
0.0
0
200
400
600
800
Transverse Position (nm)
q
Lumen
r

Figure 1. Analysis of the fluorophore NHS-ester staining pattern in expanded mouse organs. (**a**–**c**) Confocal microscopy images of fluorophore NHS-ester-labeled mouse brain slice after expansion. Inset images in **b**–**c** display a magnified view of the boxed regions. Red arrowhead in **a** indicates endoplasmic reticulum. Yellow arrowheads in **a** indicate mitochondria. Cyan arrowhead in **a** indicates nuclear membrane. **a**, Cy3 NHS ester; **b**, ATTO 647N NHS ester; **c**, Alexa Fluor 488 NHS ester. (**d**) Confocal microscopy image of the mouse brain corpus callosum after expansion. Green, Alexa Fluor 488 NHS ester; magenta, ATTO 647N NHS ester. The inset image displays a magnified view of the boxed region. (**e**) Confocal microscopy image of the expanded mouse heart slice labeled with Alexa Fluor 488 NHS ester and ATTO 647N NHS ester. Green, Alexa Fluor 488 NHS ester; magenta, ATTO 647N NHS ester. Blue arrowhead indicates cardiac muscle cells. Yellow dotted circles indicate capillaries. Yellow arrowheads indicate mitochondria. (**f**) Confocal microscopy image of mouse brain CA1, CA2, and CA3 in the hippocampus after expansion. Green, Homer1; cyan, Bassoon; magenta, Cy3 NHS ester. White arrowheads in **f** possibly indicate synaptic vesicles at the pre-synaptic end. (**g**–**m**) Confocal microscopy images of the mouse liver slice after expansion. Gray, ATTO 647N NHS ester; blue, DAPI. (**g**) General histology of the expanded liver with inter-digestion staining with ATTO 647N NHS ester. PV, portal vein; CV, central vein. Gray arrowheads indicate sinusoids. Green arrowheads indicate binuclear hepatocytes. **g**–**i**, inter-digestion staining; **j**–**k**, pre-gelation staining; **l**–**m**, post-digestion staining. (**i**) Magnified view of the boxed region in **h**. (**k**) Magnified view of the boxed region in **j**. (**m**) Magnified view of the boxed region in **l**. Yellow arrowheads in **i**, **k**, **m** indicate mitochondria. Red arrowheads in **i**, **k**, **m** indicate Golgi apparatus. (**n**–**r**) ExM imaging of the mouse small intestine slice after expansion. Gray, ATTO 647N NHS ester; blue, DAPI. Magenta arrowheads indicate goblet cells. Yellow arrowheads indicate mitochondria. Cyan arrowheads indicate brush border. **n**–**o**, inter-digestion staining; **q**–**r**, pre-gelation staining. (**o**) Magnified view of the boxed region in **n**. (**p**) Multiple-peak Gaussian-fitted line profile of microvilli along the magenta line in **o**. (**r**) Magnified view of the boxed region in **q**. Scale bars: (**a**) 2 µm; (**b**–**c**) 5 µm; (**d**) 20 µm; insets in (**b**–**d**) 500 nm; (**e**) 10 µm; (**f**) 5 µm; inset in (**f**) 1 µm; (**g**) 100 µm; (**h**) 5 µm; (**i**) 1 µm; (**j**) 5 µm; (**k**) 1 µm; (**l**) 5 µm; (**m**) 1 µm; (**n**) 10 µm; (**o**) 1 µm; (**q**) 10 µm; (**r**) 1 µm. All length scales are presented in pre-expansion dimensions.

In contrast, hydrophilic fluorophore NHS esters, such as Alexa Fluor 488 NHS ester, strongly labeled the nucleoplasm and showed uniform staining in the cytoplasm, as shown in **Fig. 1c**. Other hydrophobic and hydrophilic fluorophore NHS esters showed similar staining patterns, as shown in **Supplementary Fig. 1**. We investigated whether other physicochemical properties of fluorophores, such as their charges, affected their staining pattern. Both ATTO 565 and Cy3 had a zero net-charge; however, ATTO 565 was more hydrophilic than Cy3. These two fluorophore NHS esters showed completely different staining patterns, as shown in **Supplementary Fig. 1f**,**h**, indicating that hydrophobicity was the key factor determining the labeling pattern of the fluorophore NHS esters. In addition, a recent study has reported that the hydrophobicity of fluorophores, not their charge, determines the non-specific binding of fluorophore-conjugated antibodies during single-molecule imaging[31]. The difference in the staining patterns being dependent on the hydrophobicity of the fluorophores indicated that the local environment around the primary amines of proteins would affect the labeling density of the fluorophore NHS esters. Hydrophobic fluorophore NHS esters preferentially labeled lipid-rich structures, such as the nuclear membrane, mitochondria, ER, and myelinated fibers, indicating that the use of a single fluorophore NHS ester would not be sufficient to visualize all anatomically relevant protein structures.

Next, we used both hydrophobic and hydrophilic fluorophore NHS esters to label single specimens. In the mouse brain corpus callosum, where many myelinated nerve fibers are present[32], Alexa Fluor 488 NHS ester labeled the axons of the myelinated fibers, while ATTO 647N labeled the surrounding myelin, as shown in **Fig. 1d**. Alexa Fluor 488 NHS ester visualized a greater number of anatomical structures than ATTO 647N NHS ester does in the mouse heart. Alexa Fluor 488 NHS ester visualized the anatomy of cardiac muscle cells, including structures and components such as the Z disc, A band, M line, and capillaries. In contrast, ATTO 647N NHS ester showed strong labeling of mitochondria (**Fig. 1e**). To perform the aforementioned experiment, the mouse brain and heart slices were first permeabilized with Triton X-100, followed by fluorophore NHS-ester labeling or gelation. The compatibility of our labeling technique with permeabilization enabled the co-staining of specimens with antibodies and fluorophore NHS esters. When a mouse brain slice was stained with Cy3 NHS ester and antibodies against the pre-synaptic marker Bassoon and post-synaptic marker Homer1, Cy3 NHS ester exhibited a band-like structure located between Homer1 and Bassoon but was more closely located to and overlapped with Bassoon (**Fig. 1f**; see **Supplementary Fig. 3a–d** for more images). Such localization of Cy3 NHS ester close to the pre-synapse can be attributed to the staining of lipid-rich synaptic vesicles at the pre-synapses. We recently showed that F-actin is mainly localized in post-synaptic densities[33]. By combining hydrophobic fluorophore NHS-ester labeling and the ExM imaging of actin, we visualized the four-layered structures of Bassoon, hydrophobic fluorophore NHS ester, Homer1, and F-actin (**Supplementary Fig. 3e–j**). The range of the structures visualized using the fluorophore NHS-ester labeling varied depending on the specimen type and fixation. As shown in **Supplementary Fig. 4a**, cytoskeletons, which were not visible in the mouse brain and heart, were observed in cultured HeLa cells fixed with 4% paraformaldehyde (PFA). However, cytoskeletons were not observed when the same cells were fixed with PFA and glutaraldehyde (GA), as shown in **Supplementary Fig. 4b**.

Visualization of the anatomical structures of various mouse organs through the inter-digestion staining of fluorophore NHS esters

Next, we optimized the fluorophore NHS-ester labeling process to label more anatomically relevant structures in diverse mouse organs. The expansion of mouse organ slices, such as the kidney, has been recently demonstrated[34]. Repetitive digestion using proteinase K at 37 °C enabled more than a four-fold expansion of diverse mouse organ slices with a thickness of 1 mm, including the heart, kidney, liver, lung, small intestine, spleen, and stomach (**Supplementary Fig. 5**; see **Methods** for detailed protocol). Next, we aimed to determine when it would be optimal to apply fluorophore NHS esters in such a repetitive digestion process. We compared the images of specimens prepared using three different protocols: first, the specimens were labeled with fluorophore NHS ester and then embedded in a hydrogel. This process was called pre-gelation. Second, specimens were embedded in hydrogels, digested with proteinase K briefly (approximately 4 h), labeled with fluorophore NHS esters, and further digested with proteinase K. This process was called inter-digestion. Third, the specimens were embedded in hydrogels, repetitively digested, and labeled with fluorophore NHS esters. This process was called post-digestion. Among these three processes, inter-digestion visualized the most diverse structures. In the mouse liver, both the pre-gelation and inter-digestion processes visualized mitochondria; however, only inter-digestion showed the Golgi apparatus (**Fig. 1g–m**, see **Supplementary Fig. 6** for a larger field-of-view image). In addition, the fluorescence signal intensity observed after the pre-gelation process was several-fold lower than that observed after inter-digestion. This was attributed to the bleaching of the fluorophores during the *in situ* gelation during the pre-gelation process. Post-digestion did not show any clear cellular organelles, as these structures were over-digested and may have lost their structural integrity. In the mouse intestine, the inter-digestion process visualized individual microvillus of the brush borders that were not clearly observed *via* pre-gelation (**Fig. 1n–r**). The superior labeling performance of the inter-digestion process could be explained by the exposure of primary amines buried in proteins after the first brief digestion. During pre-gelation, the specimens were first treated with fluorophore NHS esters and then with AcX. As both fluorophore NHS esters and AcX reacted with primary amines, some proteins did not have enough fluorophore NHS esters for visualization nor AcX for anchoring at the same time. On the contrary, during inter-digestion, newly exposed primary amines could be available for labeling, and more diverse structures would be labeled and visualized. Such exposed primary amines would also increase the fluorescence signal by providing a greater number of labeling sites.

We applied the inter-digestion process of fluorophore NHS-ester labeling to various mouse organs, such as the liver (**Fig. 1g–m**, **Supplementary Fig. 6**), esophagus (**Supplementary Figs. 7–8**, **Supplementary Video 4**), stomach (**Supplementary Figs. 9–10**, **Supplementary Video 5**), small intestine (**Fig. 1n–r**, **Supplementary Figs. 11–12**, **Supplementary Video 6**), kidney (**Supplementary Fig. 13**, **Supplementary Video 7**), lung (**Supplementary Figs. 14–15**, see **Supplementary Video 8** for a z-stack image and **Supplementary Video 9** for a three-dimensional view), heart (**Fig. 1e**, **Supplementary Fig. 16**, **Supplementary Video 10**), and testis (**Supplementary Fig. 17**, **Supplementary Video 11**). In these mouse organs, we found that inter-digestion staining with fluorophore NHS esters revealed not only macroscopic histological features but also subcellular structures and organelles (**Supplementary Notes 1–2**). More importantly, structures including the basal striation (**Supplementary Fig. 13c**), foot process (**Supplementary Fig. 13d**), outer membranes of individual mitochondria of the kidney (**Supplementary Fig. 13f**), the secretory granules (lamellar bodies) needed to distinguish between alveolar cell types I and II of the lung (**Supplementary Fig. 15**), individual microvillus of the brush border (**Fig. 1o**), secretory vesicles of goblet cells in the small intestine (**Supplementary Fig. 12**), and individual mitochondria and Golgi apparatus of the liver (**Supplementary Fig. 6**) that cannot be identified or visualized with optical microscopy and thus require electron microscopy imaging were clearly visualized with diffraction-limited confocal microscopy.

Development of whole-ExM

Next, we attempted to visualize all anatomical structures of the whole zebrafish larvae, which have been widely used as a vertebrate model as they demonstrate higher genetic similarity to humans than *C. elegance* or *Drosophila*[35]. However, when the staining and expansion protocol developed for mouse organ slices was applied to zebrafish larvae, two problems were observed. First, after repetitive proteinase digestion, relatively dense body parts of the whole larvae, such as the eyes and craniofacial bones, disappeared. Second, the larvae were expanded only 2.3-fold in the presence of calcified hard components, such as bones, cartilages, and calcified tissues, at 6 days post-fertilization (dpf).

The first problem could probably be attributed to the limited diffusion of materials, such as AcX, hydrogel monomers, polymerization initiators, and catalysts. To solve this problem, we added a surfactant (0.05% to 0.1% Triton X-100) to the AcX solution and hydrogel solution to accelerate the diffusion of these materials deep into the specimens. More importantly, we used the thermal initiator 2,2'-azobis[2-(2-imidazolin-2-yl)propane]dihydrochloride (VA-044) instead of a mixture of ammonium persulfate (APS), tetramethylethylenediamine (TEMED), and 4-hydroxy-2,2,6,6-tetramethylpiperidin-1-oxyl (H-TEMPO) and extended the incubation time of the larvae in the hydrogel solution to 18 h. Such prolonged incubation was not possible with a hydrogel solution containing APS, TEMED, and H-TEMPO, as hydrogels were formed after 1 h of incubation—even at 4 °C. We also incubated the whole larvae in a hydrogel solution containing only TEMED and H-TEMPO for more than 10 h. Subsequently, the larvae were incubated with a hydrogel solution containing APS, TEMED, and H-TEMPO briefly, which was followed by gelation at 37 °C. In this protocol, hydrogels were not formed after the first incubation, but the hard organs still disappeared after digestion. This indicated that hydrogels were not formed in these areas, and proteins present in these organs were digested and washed away. Through these two modifications, including the addition of a surfactant to the AcX and hydrogel solutions and the use of VA-044, all organs of the whole zebrafish larvae were preserved after expansion. However, these modifications alone were not sufficient to uniformly expand the larvae.

We introduced a decalcification process to uniformly expand the whole larvae by more than 4-fold. The calcification of bones and cartilages starts at 3 dpf in zebrafish larvae[36], and such calcified structures resisted full expansion. For decalcification, we initially treated chemically fixed larvae with 0.5 M ethylenediaminetetraacetic acid (EDTA), which is widely used in histology and bone clearing for decalcification[37]. Following decalcification, the larvae were embedded in a hydrogel, treated with proteinase multiple times, and then expanded. However, this process showed only a 2.7-fold expansion (**Supplementary Fig. 18**). The extension of the EDTA treatment for up to three weeks did not yield a higher expansion factor. The decalcification process was then applied after digestion. The larvae were embedded in a hydrogel without any decalcification process, digested multiple times, and then treated with a decalcification buffer containing 1 M NaCl. Sodium chloride was added to the decalcification buffer to prevent the expansion of the digested larvae before the complete removal of the calcium ions. This protocol, which applied the decalcification process after digestion, yielded a 4.1-fold expansion (**Supplementary Fig. 18**, see **Supplementary Fig. 19** for a comparison between proExM and whole-ExM) of larvae aged 3–12 dpf. Full expansion of the larvae with post-digestion decalcification indicated that proteinase treatment rendered the calcium ions more accessible to EDTA and thus enabled their complete removal.

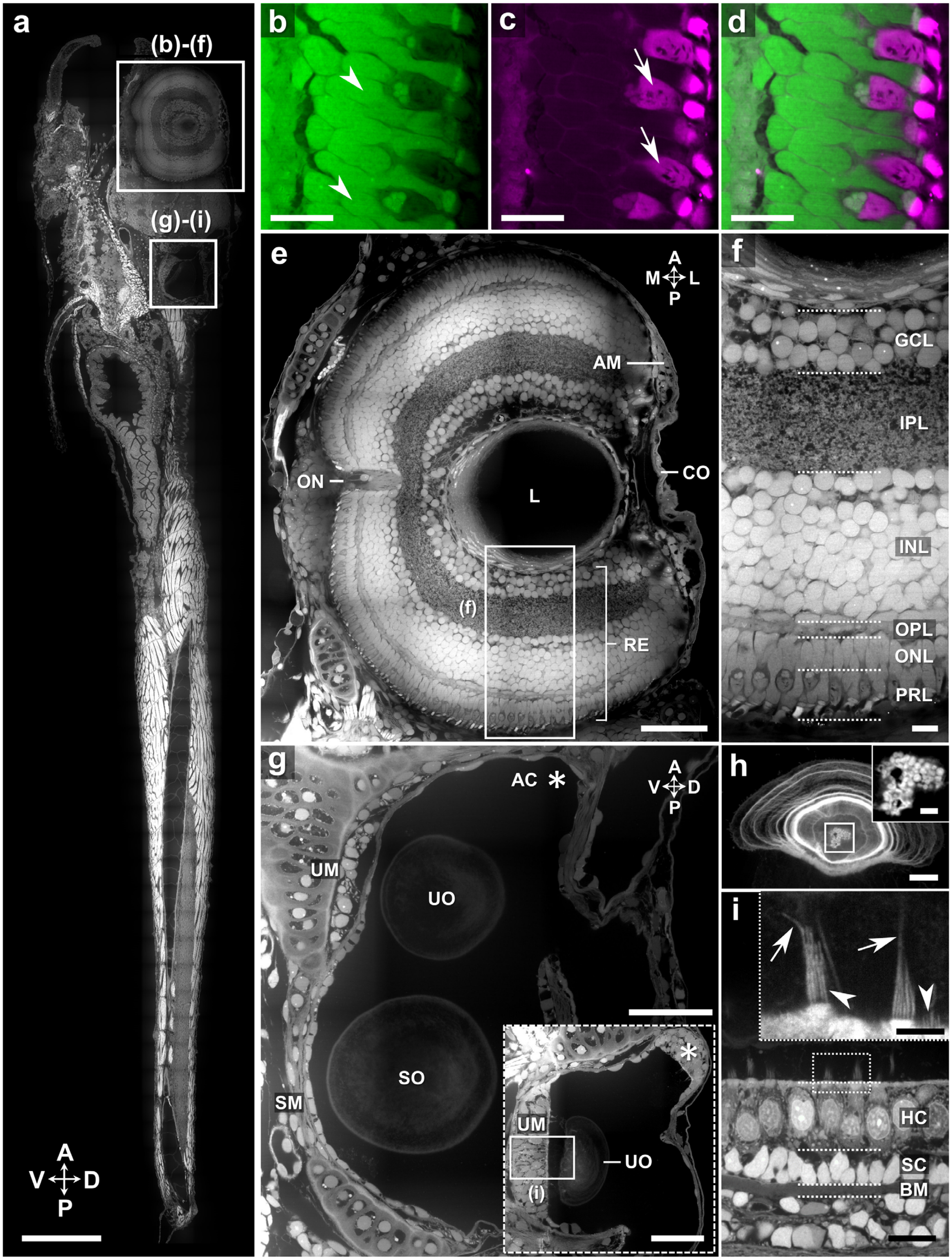
a
(b)-(f)
(g)-(i)
A
V
D
P
b
c
d
e
A
M
L
P
AM
CO
ON
L
(f)
RE
f
GCL
IPL
INL
OPL
ONL
PRL
g
AC
A
V
D
P
UM
UO
SO
SM
UM
UO
(i)
h
i
HC
SC
BM

263

Figure 2. Whole-ExM imaging of zebrafish larvae. (**a**) Confocal microscopy image of an expanded 6 dpf larval zebrafish. (**b–d**) Different staining patterns of Alexa Fluor 488 NHS ester (green) and ATTO 647N NHS ester (magenta) in labeling photoreceptor cells. Cell bodies (arrowheads) were labeled more intensely with Alexa Fluor 488 NHS ester, while outer segments (arrows) were stained more intensely with ATTO 647N NHS ester. (**e**) Montage image of the larval eye showing major features of the vertebrate eye, including the angle mesenchyme (AM), optic nerve (ON), lens (L), cornea (CO), and retina (RE) layers. (**f**) Magnified view of the boxed region in **e**, showing the retinal sections that organized into highly structured layers, including the ganglion cell layer (GCL), inner plexiform layer (IPL), inner nuclear layer (INL), outer plexiform layer (OPL), outer nuclear layer (ONL), and photoreceptor layer (PRL). (**g**) Sagittal view of the inner ear of the zebrafish larva. Two extracellular biomineral particles, utricular otolith (UO) and saccular otolith (SO), were visualized together with three sensory patches: the anterior crista (AC, asterisk), utricular macula (UM), and saccular macula (SM). The anterior crista and utricular macula with different *z*-planes are also shown in the right lower dotted box. (**h**) Sagittal view of the otolith in which the layered biomatrix is intensely stained with ATTO 647N NHS ester. The boxed region shows the inner globular structures and is shown in the magnified view in the inset box. (**i**) Frontal view of the otic sensory epithelium (utricular macula), which is made up of three essential layers: hair cells (HC), supporting cells (SC), and the basilar membrane (BM). The inset shows the magnified view of the boxed region (taken from a different sample) and reveals the brush-like sensory hair cell bundles. Arrows, kinocilia; arrowheads, stereocilia. Labels: (**a**), (**b**), (**e**), (**f**), (**g**), inset in (**g**), Alexa Fluor 488 NHS ester; (**c**), (**h**), inset in (**h**), (**i**), inset in (**i**), ATTO 647 NHS ester; (**d**) Alexa Fluor 488 NHS ester and ATTO 647N NHS ester. Scale bars: (**a**) 250 µm; (**b–d**) 10 µm; (**e**) 50 µm; (**f**) 10 µm; (**g**) and inset in (**g**) 20 µm; (**h**) 5 µm; inset in (**h**) 1 µm; (**i**) 5 µm; inset in (**i**) 2 µm. All length scales are presented in pre-expansion dimensions.

Whole-ExM imaging of whole zebrafish larvae

By combining the inter-digestion staining of fluorophore NHS esters and the expansion protocol optimized for the whole zebrafish larvae, we successfully imaged all biologically relevant structures in the whole larvae after expansion. Briefly, the process started with the fixation of the whole larvae with 4% PFA, which was followed by incubation in AcX solution containing 0.1% Triton X-100. Subsequently, the larvae were incubated in hydrogel solution containing VA-044 as initiator for more than 18 h at 4 °C and subjected to gelation at 37 °C. After hydrogel synthesis, the larvae-hydrogel composites were digested with proteinase K for 18 h, stained with fluorophore NHS esters, and further digested. After digestion, the larvae-hydrogel composites were decalcified and then expanded 4.1-fold in deionized water (see **Methods** for expansion factor determination and reproducibility). The expanded zebrafish larvae became transparent, enabling the imaging of the whole larvae without any sectioning (**Supplementary Fig. 18**). The whole process, called whole-ExM, took approximately a week to perform for 6 dpf larvae. We used spinning-disk confocal microscopy, which can acquire high-resolution images several-fold faster than point-scanning confocal microscopy to image the expanded larvae. The image acquisition of a single z-plane of the whole larvae with a resolution of 62.5 nm (250 nm / 4 = 62.5 nm) took five min (see **Fig. 2a** for the image and

Supplementary Video 1 for the annotated image). Three-dimensional imaging of a whole larvae with the same resolution would require approximately five days (see **Supplementary Fig. 20** for the whole expansion and imaging process; see **Supplementary Note 3** for details on imaging time). Both wild-type and transparent Casper zebrafish larvae were used in this study; however, no significant difference was observed in post-expansion imaging between the two lines. To confirm that the larvae were expanded homogeneously, we measured the length of the sarcomere of skeletal muscle fibers in the anterior trunk and compared it with the sarcomere length measured from electron microscopy images of larvae reported in previous studies. The average sarcomere length measured from four expanded larvae was 1.95 ± 0.12 μm. We also measured the sarcomere length in other body parts, such as the craniofacial regions, posterior trunks, and tails, but no difference was observed. The average sarcomere length measured from two independent studies on the electron microscopy imaging of larvae was 1.87 ± 0.07 μm[38,39]. Considering that these two values were measured from separate specimens and muscles are more resistant to expansion than other tissues[40], the good agreement between these two values (4.3% difference) indicates that the expansion was homogeneous and the whole-ExM process preserved not only the morphology of the structures but also their physical dimensions (**Supplementary Fig. 21**).

In the zebrafish larvae, the hydrophilic fluorophore NHS ester (Alexa Fluor 488 NHS ester) and hydrophobic fluorophore NHS ester (ATTO 647N NHS ester) demonstrated different staining patterns. Alexa Fluor 488 NHS ester outlined most of the biologically relevant structures with similar intensities, making it useful for determining their overall morphologies (**Fig. 2a**). In contrast, ATTO 647N NHS ester strongly stained lipid-rich structures and revealed detailed organelle structures, thereby enabling the distinction of different cell types or subcellular structures (**Supplementary Fig. 22**). In the retinal layers, photoreceptors were uniformly stained with Alexa Fluor 488 NHS ester; however, the lipid-rich outer segments, which consist of a stack of disk membranes, were strongly stained with ATTO 647N NHS ester (**Fig. 2b–d**, see **Supplementary Video 12** for a z-stack image)[41]. In addition, the cornea, lens, retinal layers, and optic nerves were clearly identified in the eye (**Fig. 2e–f**), and the otoliths and sensory patches of the inner ear (**Fig. 2g**, see **Supplementary Video 13** for a z-stack image) were also clearly visualized with Alexa Fluor 488 NHS ester. Individual otolithic membrane layers composed of the otolith and three cell layers of the otic sensory epithelium were difficult to identify with Alexa Flour 488 NHS ester but were clearly visualized with ATTO 647N NHS ester (**Fig. 2h–i**). For cilia present in the hair cell bundles of the inner ear (dotted rectangle in **Fig. 2i**), the average center-to-center distance between neighboring cilia is smaller than 150 nm[42], and the distinction of individual cilia requires a resolution beyond that of optical microscopy. As shown in the inset of **Fig. 2i**, the resolution of whole-ExM was sufficiently high to visualize individual cilium of the hair cell bundles and distinguish between kinocilium (relatively long cilium; white arrows in **Fig. 2i**) and stereocilia (relatively short cilia; white arrowheads in **Fig. 2i**) based on their length.

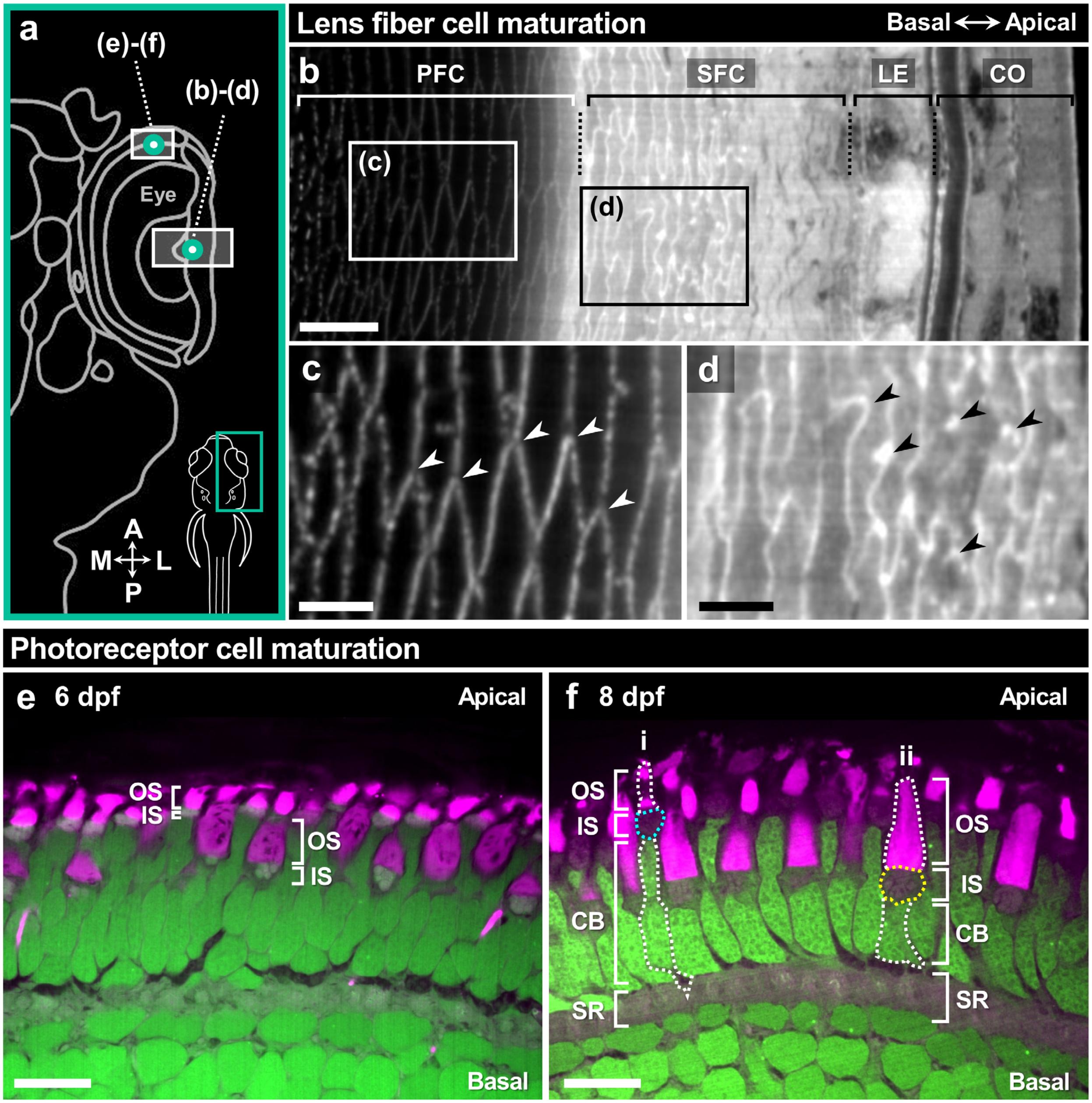
a
(e)-(f)
(b)-(d)
Eye
A
M
L
P
Lens fiber cell maturation
Basal ⟷ Apical
b
PFC
SFC
LE
CO
(c)
(d)
c
d
Photoreceptor cell maturation
e 6 dpf
Apical
OS
IS
OS
IS
Basal
f 8 dpf
Apical
i
ii
OS
IS
CB
SR
OS
IS
CB
SR
Basal

Figure 3. Whole-ExM imaging of anatomical changes in zebrafish larvae in different developmental stages. (**a**) Schematic diagram of larval zebrafish depicting locations in **b**–**f**. (**b**) Confocal microscopy image of the anterior lens of 8 dpf zebrafish larva. PFC, primary lens fiber cell; SFC, secondary lens fiber cell; LE, lens epithelium; CO, cornea. (**c**) Magnified view of the boxed region in **b**, highlighting the detailed anatomical features of PFCs. Arrowheads, Y-shaped suture pattern between the ends of cells. (**d**) Magnified view of the boxed region in **b**, showing the detailed structure of SFCs. Arrowheads, ball-and-socket inter-digitations between older fiber cells. (**e**–**f**) Confocal microscopy images of the retinal layers of larval

zebrafish at (**e**) 6 dpf and (**f**) 8 dpf, depicting photoreceptor cell maturation. Green, Alexa Fluor 488 NHS ester; magenta, ATTO 647N NHS ester. OS, outer segment; IS, inner segment; CB, cell body; SR, synaptic region. For **e**, the same image shown in **Fig. 2d** is used. Labels: (**b**–**d**), ATTO 647N NHS ester; (**e**–**f**), Alexa Fluor 488 NHS ester and ATTO 647N NHS ester. Scale bars: (**b**) 5 µm; (**c**–**d**) 2 µm; (**e**–**f**) 10 µm. All length scales are presented in pre-expansion dimensions.

Use of whole-ExM to study anatomical changes in different developmental stages

Whole-ExM was useful in studying the changes in the morphologies of anatomical landmarks during different developmental stages. Among several examples, we focused on two cases: fiber cell maturation in the lens and photoreceptor cell maturation in the retina (**Fig. 3a**). In the anterior segment of the lens in 8 dpf larva, highly organized layers of the lens fiber cells, lens epithelium, and cornea were distinguished with ATTO 647N NHS-ester labeling (**Fig. 3b**). During lens maturation, fiber cells can be classified into two cell types depending on their degree of maturation: primary lens fiber cells (PFCs) and secondary lens fiber cells (SFCs). Both cells lack cellular organelles. PFCs are found close to the core of the lens, and SFCs are found in the more peripheral regions of the lens. PFCs show well-ordered hexagonal cellular arrangements, whereas SFCs show less ordered arrangements and unique protrusions formed *via* the ball-and-socket process. In addition, SFCs are more mature, denser, and less transparent than PFCs[43]. We were able to classify these two different types of fiber cells based on their detailed anatomical features (**Fig. 3c**–**d**), such as the hexagonal profile of PFCs and the ball-and-socket junction of SFCs.

Photoreceptor maturation in the retinal layer is another interesting example. At 6 dpf, two rows of inner segments were visible (**Fig. 3e**). At 8 dpf, an increase in the length of the outer segments was observed, but the extent of this increase differed depending on the photoreceptor subtype (**Fig. 3f**). In addition, two distinct rows of inner segments became more evident (**Fig. 3f**; see **Supplementary Fig. 23** for each fluorophore channel; see **Supplementary Video 12** for z-stack image of 8 dpf larval retina). Based on these morphological features, we were able to classify the photoreceptor cells into two different subtypes: double cone photoreceptor cells, which are characterized by shorter outer segments (cell i in **Fig. 3f**), and single cone photoreceptor cells or rod photoreceptor cells, which are characterized by a long outer segment (cell ii in **Fig. 3f**). The observations were in agreement with those of previous studies on zebrafish retina[41–44].

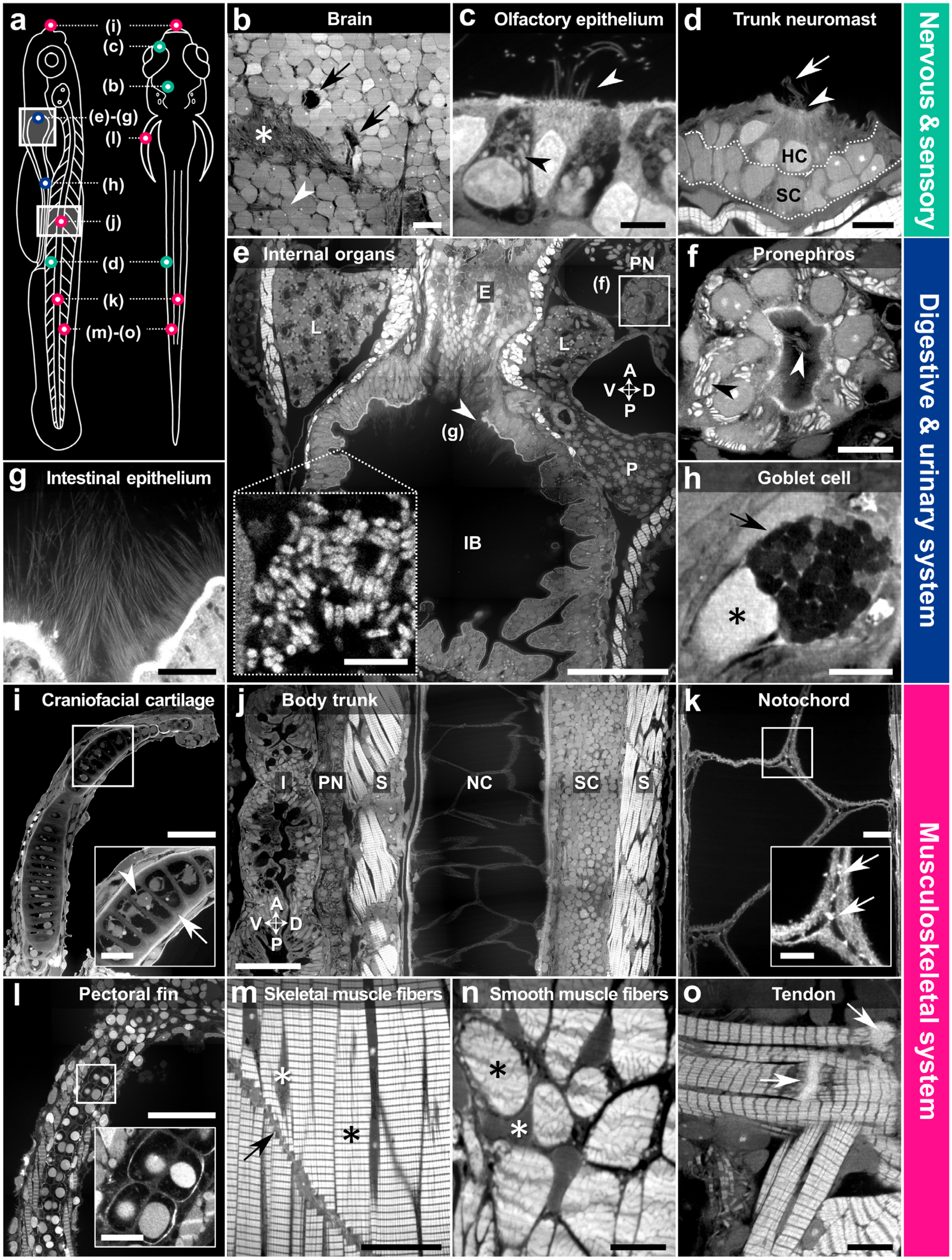
a
(i)
(c)
(b)
(e)-(g)
(l)
(h)
(j)
(d)
(k)
(m)-(o)
b
Brain
c
Olfactory epithelium
d
Trunk neuromast
HC
SC
Nervous & sensory
e
Internal organs
PN
(f)
E
L
L
A
V
D
P
(g)
P
IB
f
Pronephros
g
Intestinal epithelium
h
Goblet cell
Digestive & urinary system
i
Craniofacial cartilage
j
Body trunk
I
PN
S
NC
SC
S
A
V
D
P
k
Notochord
Musculoskeletal system
l
Pectoral fin
m
Skeletal muscle fibers
n
Smooth muscle fibers
o
Tendon

Figure 4. Whole-ExM imaging of a variety of key landmarks in zebrafish larvae. (**a**) Schematic diagram of lateral and dorsal views of larval zebrafish depicting locations in **b**–**o**. Highlighted structural landmarks are color-coded based on the organ system to which they belong. (**b**–**d**) Confocal microscopy images of major organs that belong to the nervous or sensory system. (**b**) Brain. Arrowhead, nucleus; arrows, blood vessels; asterisk, cytoplasm. (**c**) Olfactory sensory epithelium. Black arrowhead, mitochondria; white arrowhead, cilia. (**d**) Trunk neuromast. HC, hair cell; SC, supporting cell. Arrow, kinocilium; arrowhead, stereocilia. (**e**) Internal organs that belong to the digestive or urinary system. E, esophagus; L, liver; IB, intestinal bulb; P, pancreas; PN, pronephros. The dotted box highlights bacterial colonies attached to the intestinal bulb epithelium (observed in a different sample). (**f**) Magnified view of the boxed region in **e**, showing the frontal view of the pronephros. White arrowhead, motile cilia; black arrowhead, mitochondria. (**g**) Unusually long (~ 20 μm) microvilli found in the anterior intestinal bulb region adjacent to the esophageal intestinal junction. (**h**) Goblet cells in mid-intestine. Arrow, secretory vesicle; asterisk, nucleus. (**i**–**o**) Confocal microscopy images of representative components that belong to the musculoskeletal system. (**i**) Craniofacial cartilage. The inset highlights a chondrocyte (arrowhead) encapsulated by a cartilage matrix (arrow). (**j**) Body trunk. I, intestine; PN, pronephric duct; S, skeletal muscle; NC, notochord; SC, spinal cord. (**k**) Magnified view of the notochord organized by vacuoles, sheath cells, and tightly apposed notochordal vacuolated cells. The inset highlights caveolae (arrows) between neighboring notochordal cells. (**l**) Pectoral fin comprising the fin membrane, skeletal muscle fibers, and endoskeletal core disk. The inset shows divided chondrocytes forming symmetrical cell nests. (**m**) Magnified view of the skeletal muscles. White asterisk, nucleus; black asterisk, muscle fibers; black arrow, connective tissue. (**n**) Frontal view of the smooth muscle fibers on the peripheral edge of the internal organs. Black asterisk, muscle fibers; white asterisk, nucleus. (**o**) Tendons (arrows) between the cartilaginous bone and muscle fibers. Except for **i**, which was observed with an 8 dpf larva, the remaining images were observed with 6 dpf larvae. Labels: (**b**), (**c**), (**d**), (**e**), (**f**), (**j**), (**n**), Alexa Fluor 488 NHS ester; (**g**), (**h**), (**i**), (**k**), (**l**), (**m**), (**o**), ATTO 647 NHS ester. Scale bars: (**b**) 5 μm; (**c**) 2 μm; (**d**) 5 μm; (**e**) 100 μm; inset in (**e**) 5 μm; (**f**–**g**) 10 μm; (**h**) 5 μm; (**i**) 50 μm; inset in (**i**) 10 μm; (**j**) 100 μm; (**k**) 10 μm; inset in (**k**) 5 μm; (**l**) 50 μm; inset in (**l**) 10 μm; (**m**) 20 μm; (**n**) 5 μm; (**o**) 10 μm. All length scales are presented in pre-expansion dimensions.

Nanoscale imaging of diverse organs of whole larvae

Whole-ExM visualized physiological details in a diverse range of tissues and organs across the whole larvae (**Fig. 4a**). In the nervous systems, the brain (**Fig. 4b**) and the spinal cord (**Supplementary Fig. 24**) were visualized. In the sensory systems, the nanoscale details of major sensory organs, such as the individual microvillus of the olfactory sensory epithelium (**Fig. 4c**, see **Supplementary Fig. 25** for more detailed analysis and **Supplementary Video 14** for a z-stack image) and the individual cilium and cells of trunk neuromast (**Fig. 4d**, see **Supplementary Fig. 26** for detailed analysis and **Supplementary Videos 15** for a z-stack image) were visualized. In the digestive and urinary systems, most features of organ morphogenesis that are commonly observed in this developmental stage were clearly observed along with the detailed shape of major internal organs, including the intestinal bulb, liver, pancreas, esophagus (**Fig. 4e**), pronephros (the earliest stage of kidney development; **Fig. 4f**), and pronephric duct along the whole body (**Supplementary Fig. 27**). Interestingly, structures presumably of bacteria were also observed inside the intestinal bulb (inset of **Fig. 4e**, see **Supplementary Fig. 28a–e** for detailed analysis and **Supplementary Video 16** for a z-stack image). Whole-ExM clearly visualized the microvilli of the intestinal epithelium (**Fig. 4g**, see **Supplementary Video 17** for a z-stack image) and the details of the mid-intestine with goblet cells (**Fig. 4h**, see **Supplementary Video 18** for a z-stack image). Whole-ExM also successfully visualized complex musculoskeletal tissues (**Supplementary Video 19**), such as calcified cartilages (**Fig. 4i**, see **Supplementary Fig. 29** for the whole pharyngeal arches); body trunk, including the spinal cord and notochord (**Fig. 4j** for a large field of view and **Fig. 4k** for the notochord; see **Supplementary Fig. 30** for the body trunk of the more distal region and **Supplementary Video 20** for a z-stack image of notochord); fins (**Fig. 4l**, see **Supplementary Video 21** for a z-stack image); muscle fibers (**Fig. 4m–n,** see **Supplementary Fig. 31** for a detailed analysis); and even tendons (**Fig. 4o**).

Moreover, whole-ExM enabled the visualization of nanoscale details of certain anatomical structures that cannot be clearly imaged with diffraction-limited microscopy. These structures include not only individual cilium (and the distinction between kinocilium and stereocilia) in the trunk neuromast (**Fig. 4d**, **Supplementary Fig. 26**) but also microscopic protuberances or membrane protrusions directly related to organ function. Such structures include motile cilia found in the pronephric duct (**Fig. 4f**, **Supplementary Fig. 27**) or microvilli in the intestinal bulb (**Fig. 4g**), secretory vesicles in goblet cells (**Fig. 4h**), dense caveolae in the membrane of adjacent notochordal cells (**Fig. 4k**), and mitochondria in skeletal muscle fibers (**Fig. 4m**, **Supplementary Fig. 31**). As the whole-ExM process non-specifically labeled proteins, it showed structures that have not been reported previously. For example, the presence of long microvilli located at the esophageal intestinal junction (**Fig. 4g**, see **Supplementary Fig. 28f–g** for details and **Supplementary Video 17** for a z-stack image) has not been reported previously, to our knowledge. Interestingly, we observed an unknown structure smaller than a single cell with characteristic needle-like structures stretched inside. This unknown structure was only found in the externally exposed regions in the zebrafish larvae, such as the olfactory epithelium and skin, and was found inside other cells (**Supplementary Fig. 32**). This structure might be an unknown cell subtype, an unknown appearance of the differentiating cell, or an infected cell with a parasitic protist, such as apicomplexan.

Imaging of the fluorescent proteins of transgenic zebrafish by whole-ExM

Finally, we investigated whether fluorescence signals from genetically encoded fluorescent proteins could be retained during the whole-ExM process. Recently, it has been reported that some fluorescent proteins (i.e., GFP, mCherry, and TagRFP) retain their fluorescence signals after a 48 h-long proteinase K digestion, and they can even be labeled with antibodies to boost their fluorescence signals[14]. As reported, we successfully imaged the fluorescence signal of GFP in transgenic zebrafish lines after a 54 h-long proteinase K digestion, as shown in **Supplementary Fig. 33a–c**. The fluorescence signals were boosted by labeling GFP with antibodies after a 54 h-long digestion, as shown in **Supplementary Fig. 33d–g**. The dense staining of ATTO 647N did not interfere with the GFP signal, and these two signals were simultaneously visualized, as shown in **Supplementary Fig. 33e–f**. Whole-ExM was also compatible with mRNA imaging. As shown in **Supplementary Fig. 34**, the whole-ExM protocol combined with expansion fluorescent *in situ* hybridization (ExFISH)[22] visualized the mRNA puncta at an elevated resolution, enabling nanoscale transcriptional analysis over the whole larvae.

High-precision registration of images using fluorophore NHS-ester staining as fiducial markers

We found another use of fluorophore staining in addition to the visualization of major biological structures in mouse organs and zebrafish larvae. The dense labeling of ATTO 647N NHS ester and Cy3 NHS ester enabled the registration of images acquired *via* repetitive staining and imaging with less than a 10-nm registration error (see **Supplementary Note 4** for detailed procedure). Recently developed multiplexed tissue imaging techniques based on tissue expansion rely on repetitive staining and imaging, which require registration between images acquired at different imaging rounds[20,45,46]. DAPI-stained nuclei have been widely used as fiducial markers[45,46]. Here, we found that registration using DAPI as a fiducial marker yielded a registration error larger than 50 nm, especially when the density of the nucleus was low (**Supplementary Fig. 35f,g,m**). Hydrogel shrinking and expansion during buffer exchange and hydrogel handling during repetitive staining and imaging generated non-linear deformation in the specimen, resulting in such a registration error where the nucleus was absent. However, when Cy3 NHS-ester staining was used as a fiducial marker for the repetitive imaging of an expanded mouse brain slice, a registration error less than 10 nm was achieved, as shown in **Supplementary Fig. 35h,i,o**. We found that Cy3 NHS ester was more favorable than ATTO 647N NHS ester as a fiducial marker, as the excitation and emission spectra of ATTO 647N embedded in a hydrogel were blue-shifted when they were exposed to excitation lasers for an extended period of time (**Supplementary Figs. 36–37**, see **Supplementary Note 5** for details)[47]. Cy3 NHS ester also enabled three-dimensional registration between two z-stack images of an expanded brain slice acquired from different staining and imaging rounds (**Supplementary Fig. 38**).

DISCUSSION

In this work, we demonstrated a simple protocol that enables the three-dimensional super-resolution imaging of all anatomically relevant structures in diverse mouse organs and even whole larval zebrafish *via* expansion microscopy. The key ideas here are using both hydrophobic and hydrophilic fluorophores to label all proteins, the introduction of fluorophore NHS esters after a short period of digestion, and optimized gelation and digestion protocol for mouse organs and zebrafish larvae. For mouse organs, this process would be highly useful for studying diseases featuring anatomical changes in cellular structures or organelles. In addition, this process will allow pathologists to confirm the pathologic diagnosis of diseases that require ultramicroscopic evidences in the environment without access to electron microscopy[40]. Such examples include the foot process loss in minimal change disease among nephrotic syndrome[48]; the Zebra bodies in Fabry's disease[49]; the neurosecretory granules in neuroendocrine tumors, such as pheochromocytomas[50]; and the structural abnormality of mitochondria in congenital mitochondrial myopathy[51]. For whole-organism imaging, whole-ExM would be highly useful for studying transgenic lines showing anatomical abnormalities or studying the nanoscale anatomical changes occurring in different developmental stages. As zebrafish share a high degree of genetic similarities with humans[35] and have similar anatomical structures with humans[52], whole-ExM would enable the study of the molecular mechanisms of human diseases.

The resolution of whole-ExM is lower than that of electron microscopy, but it enables three-dimensional sub-100-nm resolution imaging of all anatomical structures throughout the whole organism with a simple microscopy setup and chemical process within a relatively short period (less than 5 min for a single z-plane imaging of a whole larva) and without any antibodies. With these advantages, whole-ExM would be useful in identifying unknown structures that have not been reported by electron microscopy imaging or super-resolution imaging based on antibody labeling. For the imaging of non-fluorescent proteins, the whole-mount staining of larvae with antibodies, followed by the whole-ExM protocol, would enable the super-resolution imaging of both non-fluorescent proteins and dense fluorophore labeling. When whole-mount staining is not available because of limited antibody diffusivity, especially for larvae older than 3 dpf, simply sectioning the larvae into thick slices and staining them with antibodies followed by whole-ExM could be used. Alternatively, a post-gel staining version of whole-ExM could be developed by replacing proteinase K treatment with heat denaturation[14].

Whole-ExM would be applicable to a wide range of organisms. One of the biggest challenges in studying the nanoscale structures of organisms other than model organisms is the lack of high-affinity antibodies.

We showed here that dense fluorophore labeling combined with optimized gelation and expansion protocol could visualize all anatomically relevant structures—even without any antibodies. The general procedure of whole-ExM, which starts with permeabilization and proceeds to the extended incubation of specimens in a gel solution containing a thermal initiator followed by gelation, brief digestion, the application of both hydrophilic and hydrophobic fluorophore NHS esters, further digestion, and decalcification, would work for most vertebrates after optimizing the duration of each step.

We anticipate that whole-ExM could be used to visualize the sub-10-nm details of protein structures over the whole organism. In this work, specimens were expanded only 4-fold, but a higher expansion factor, such as 10- or even 20-fold, has been demonstrated through iterative expansion[13,30,53,54]. A larger expansion factor does not always guarantee a higher resolution due to expansion inhomogeneity or signal blurring, but recent studies have reported that expansion microscopy conserves the sub-10-nm details of protein structures[13,55,56]. Once combined with iterative expansion, whole-ExM would enable organism-level systems biology with a molecular resolution.

REFERENCES

1. Susaki, E. A. & Ueda, H. R. Whole-body and Whole-Organ Clearing and Imaging Techniques with Single-Cell Resolution: Toward Organism-Level Systems Biology in Mammals. *Cell Chem. Biol.* **23**, 137–157 (2016).

2. Liu, Z. & Keller, P. J. Emerging Imaging and Genomic Tools for Developmental Systems Biology. *Developmental Cell* **36**, 597–610 (2016).

3. Pan, C. *et al.* Shrinkage-mediated imaging of entire organs and organisms using uDISCO. *Nat. Methods* **13**, 859–867 (2016).

4. Tainaka, K. *et al.* Whole-Body Imaging with Single-Cell Resolution by Tissue Decolorization. *Cell* **159**, 911–924 (2014).

5. Yang, B. *et al.* Single-Cell Phenotyping within Transparent Intact Tissue through Whole-Body Clearing. *Cell* **158**, 945–958 (2014).

6. Rawson, S. D., Maksimcuka, J., Withers, P. J. & Cartmell, S. H. X-ray computed tomography in life sciences. *BMC Biol.* **18**, 21 (2020).

7. Mulcahy, B. *et al.* A pipeline for volume electron microscopy of the caenorhabditis elegans nervous system. *Frontiers in Neural Circuits* **12**, 94 (2018).

8. Ueda, H. R. *et al.* Tissue clearing and its applications in neuroscience. *Nature Reviews Neuroscience* **21**, 61-79 (2020). doi:10.1038/s41583-019-0250-1

9. Hildebrand, D. G. C. *et al.* Whole-brain serial-section electron microscopy in larval zebrafish. *Nature* **545**, 345–349 (2017).

10. Kasthuri, N. *et al.* Saturated Reconstruction of a Volume of Neocortex. *Cell* **162**, 648-661 (2015). doi:10.1016/j.cell.2015.06.054

11. Kubota, Y., Sohn, J. & Kawaguchi, Y. Large volume electron microscopy and neural microcircuit analysis. *Frontiers in Neural Circuits* **12**, 98 (2018). doi:10.3389/fncir.2018.00098

12. Mao, C. *et al.* Feature-rich covalent stains for super-resolution and cleared tissue fluorescence microscopy. *Sci. Adv.* **6**, eaba4542 (2020). doi:10.1126/sciadv.aba4542

13. M'Saad, O. & Bewersdorf, J. Light microscopy of proteins in their ultrastructural context. *Nat.*

Commun. (2020). doi:10.1038/s41467-020-17523-8

14. Yu, C. C. *et al.* Expansion microscopy of c. Elegans. *Elife* **9**, 1–78 (2020).

15. Karagiannis, E. D. *et al.* Expansion Microscopy of Lipid Membranes. *bioRxiv* 829903 (2019). doi:10.1101/829903

16. Sun, D. *et al.* Click-ExM enables expansion microscopy for all biomolecules. *Nat. Methods* **18**, 107–113 (2021).

17. Chen, F., Tillberg, P. W. & Boyden, E. S. Expansion Micrsocopy. *Science* **347**, 543-548 (2015). doi:10.1126/science.1260088.Expansion

18. Tillberg, P. W. *et al.* Protein-retention expansion microscopy of cells and tissues labeled using standard fluorescent proteins and antibodies. *Nat. Biotechnol.* **34**, 987–992 (2016).

19. Chozinski, T. J. *et al.* Expansion microscopy with conventional antibodies and fluorescent proteins. *Nat. Methods* **13**, 485–488 (2016).

20. Ku, T. *et al.* Multiplexed and scalable super-resolution imaging of three-dimensional protein localization in size-adjustable tissues. *Nat. Biotechnol.* **34**, 973 (2016).

21. Freifeld, L. *et al.* Expansion microscopy of zebrafish for neuroscience and developmental biology studies. *Proc. Natl. Acad. Sci.***114**, E10799-E10808 (2017). doi:10.1073/pnas.1706281114

22. Chen, F. *et al.* Nanoscale Imaging of RNA with Expansion Microscopy. *Nat. Methods* **13**, 679–684 (2016).

23. Gao, R. *et al.* Cortical column and whole-brain imaging with molecular contrast and nanoscale resolution. *Science (80-.).* **363**, eaau8302 (2019).

24. Gambarotto, D. *et al.* Imaging cellular ultrastructures using expansion microscopy (U-ExM). *Nat. Methods* **16**, 71–74 (2019).

25. Zhang, Y. S. *et al.* Hybrid Microscopy: Enabling Inexpensive High-Performance Imaging through Combined Physical and Optical Magnifications. *Sci. Rep.* **6**, 22691 (2016).

26. Lim, Y. *et al.* Mechanically resolved imaging of bacteria using expansion microscopy. *PLOS Biol.* **17**, e3000268 (2019).

27. Cheng, S. & Zhao, Y. Nanoscale imaging of E. coli cells by expansion microscopy. *Discov. (Craiova, Rom.* **7**, e98–e98 (2019).

28. Götz, R. *et al.* Expansion Microscopy for Cell Biology Analysis in Fungi. *Front. Microbiol.* **11**, 574 (2020).

29. Halpern, A. R., Alas, G. C. M., Chozinski, T. J., Paredez, A. R. & Vaughan, J. C. Hybrid Structured Illumination Expansion Microscopy Reveals Microbial Cytoskeleton Organization. *ACS Nano* **11**, 12677-12686 (2017). doi:10.1021/acsnano.7b07200

30. Park, H.-E. *et al.* Scalable and Isotropic Expansion of Tissues with Simply Tunable Expansion Ratio. *Adv. Sci.* **6**, 1901673 (2019).

31. Zanetti-Domingues, L. C., Tynan, C. J., Rolfe, D. J., Clarke, D. T. & Martin-Fernandez, M. Hydrophobic Fluorescent Probes Introduce Artifacts into Single Molecule Tracking Experiments Due to Non-Specific Binding. *PLoS One* **8**, e74200 (2013).

32. Køster, R. N., Jesper, R. & Bente, P. The total number of myelinated nerve fibers is reduced in corpus callosum in brains from patients with Alzheimer's disease. *Neurobiol. Aging* **69**, 58–64 (2018).

33. Park, C. E. *et al.* Super-Resolution Three-Dimensional Imaging of Actin Filaments in Cultured Cells and the Brain via Expansion Microscopy. *ACS Nano* **14**, 14999–15010 (2020).

34. Chozinski, T. J. *et al.* Volumetric, Nanoscale Optical Imaging of Mouse and Human Kidney via Expansion Microscopy. *Sci. Rep.* **8**, 10396 (2018).

35. Howe, K. *et al.* The zebrafish reference genome sequence and its relationship to the human genome. *Nature* **496**, 498–503 (2013).

36. Spoorendonk, K. M., Hammond, C. L., Huitema, L. F. A., Vanoevelen, J. & Schulte-Merker, S. Zebrafish as a unique model system in bone research: the power of genetics and *in vivo* imaging. *J. Appl. Ichthyol.* **26**, 219–224 (2010).

37. Greenbaum, A. *et al.* Bone CLARITY: Clearing, imaging, and computational analysis of osteoprogenitors within intact bone marrow. *Sci. Transl. Med.* **9**, eaah6518 (2017).

38. Mead, A. F., Kennedy, G. G., Palmer, B. M., Ebert, A. M. & Warshaw, D. M. Mechanical Characteristics of Ultrafast Zebrafish Larval Swimming Muscles. *Biophys. J.* **119**, 806–820

(2020).

39. Charvet, B., Malbouyres, M., Pagnon-Minot, A., Ruggiero, F. & Le Guellec, D. Development of the zebrafish myoseptum with emphasis on the myotendinous junction. *Cell Tissue Res.* **346**, 439–449 (2011).

40. Zhao, Y. *et al.* Nanoscale imaging of clinical specimens using pathology-optimized expansion microscopy. *Nat. Biotechnol.* **35**, 757 (2017).

41. Albert, A. D. & Boesze-Battaglia, K. The role of cholesterol in rod outer segment membranes. *Prog. Lipid Res.* **44**, 99–124 (2005).

42. Seiler, C. *et al.* Myosin VI is required for structural integrity of the apical surface of sensory hair cells in zebrafish. *Dev. Biol.* **272**, 328–338 (2004).

43. Schonthaler, H. B. *et al.* The zebrafish mutant bumper shows a hyperproliferation of lens epithelial cells and fibre cell degeneration leading to functional blindness. *Mech. Dev.* **127**, 203–219 (2010).

44. Branchek, T. & Bremiller, R. The development of photoreceptors in the zebrafish, Brachydanio rerio. I. Structure. *J. Comp. Neurol.* **224**, 107–115 (1984).

45. Saka, S. K. *et al.* Immuno-SABER enables highly multiplexed and amplified protein imaging in tissues. *Nat. Biotechnol.* **37**, 1080–1090 (2019).

46. Shen, F. Y. *et al.* Light microscopy based approach for mapping connectivity with molecular specificity. *Nat. Commun.* **11**, 4632 (2020). doi:10.1038/s41467-020-18422-8

47. Helmerich, D. A., Beliu, G., Matikonda, S. S., Schnermann, M. J. & Sauer, M. Photoblueing of organic dyes can cause artifacts in super-resolution microscopy. *Nat. Methods* (2021). doi:10.1038/s41592-021-01061-2

48. Vivarelli, M., Massella, L., Ruggiero, B. & Emma, F. Minimal change disease. *Clin. J. Am. Soc. Nephrol.* **12**, 332-345 (2017). doi:10.2215/CJN.05000516

49. El-Abassi, R., Singhal, D. & England, J. D. Fabry's disease. *Journal of the Neurological Sciences* **344**, 5-19 (2014). doi:10.1016/j.jns.2014.06.029

50. Eisenhofer, G. *et al.* Pheochromocytomas in von Hippel-Lindau syndrome and multiple endocrine neoplasia type 2 display distinct biochemical and clinical phenotypes. *J. Clin. Endocrinol. Metab.*

86, 1999-2008 (2001). doi:10.1210/jcem.86.5.7496

51. Vincent, A. E. *et al.* The Spectrum of Mitochondrial Ultrastructural Defects in Mitochondrial Myopathy. *Sci. Rep.* **6**, 30610 (2016). doi:10.1038/srep30610
52. Bryson-Richardson, R. J. *et al.* FishNet: an online database of zebrafish anatomy. *BMC Biol.* **5**, 34 (2007).
53. Chang, J.-B. *et al.* Iterative expansion microscopy. *Nat. Methods* **14**, 593–599 (2017).
54. Truckenbrodt, S. *et al.* X10 expansion microscopy enables 25-nm resolution on conventional microscopes. *EMBO Rep.* **19**, e45836 (2018).
55. Shi, X. *et al.* Label-retention expansion microscopy. *bioRxiv* 687954 (2019). doi:10.1101/687954
56. Zwettler, F. U. *et al.* Molecular resolution imaging by post-labeling expansion single-molecule localization microscopy (Ex-SMLM). *bioRxiv* 2020.03.12.988923 (2020). doi:10.1101/2020.03.12.988923

METHODS

Materials. All chemicals and antibodies were obtained from commercial suppliers, and detailed information is provided in **Supplementary Table 1**. The concentrations of the labeling agents, including antibodies, fluorophore NHS esters, 4′,6-diamidino-2-phenylindole (DAPI), are listed in **Supplementary Table 2**.

Cell culture. HeLa cells were cultured in chambered coverglass culture wells in Minimum Essential Media (MEM) supplemented with 10% fetal bovine serum (FBS), 1% sodium pyruvate, and 1% penicillin-streptomycin and incubated in a humidified chamber with 5% CO_2 at 37 °C.

Fixation and staining of the cells. Fixation conditions varied as previous studies utilized different conditions in labeling different subcellular structures[15]. For strong fixation, cells were briefly rinsed three times with 1× phosphate buffered saline (PBS), then fixed in 4% paraformaldehyde (PFA) and 0.1% glutaraldehyde in 1× PBS for 10 min at room temperature (RT, 20–25 °C), and washed three times with 0.1 M glycine in 1× PBS for 2 min each time, and finally washed three times with 1× PBS for 2 min each time. Cells were then treated with 0.1% sodium borohydride in 1× PBS for 7 min at RT, then washed three times with 0.1 M glycine in 1× PBS for 2 min each time, and finally washed three times with 1× PBS for 2 min each time. Cells were then permeabilized in 0.2% PBST (0.2% Triton X-100, 1× PBS) for 30 min at RT. Next, the cells were stained with ATTO 647N NHS ester in 0.2% PBST for 1 h at RT, then washed three times with 0.2% PBST for 5 min each time. For general fixation, cells were briefly rinsed three times with 1× PBS, fixed with 4% PFA in 1× PBS for 10 min at RT, then washed three times with 0.1 M glycine in 1× PBS for 2 min each time and finally washed three times with 1× PBS for 2 min each time. Fixed cells were then permeabilized and stained with ATTO 647N NHS ester as described above. Cell expansion was performed as described in proExM protocol[18].

Mouse perfusion. All experimental methods involving mice were approved by the Korea Advanced Institute of Science and Technology Institutional Animal Care and Use Committee (KAIST-IACUC). Mice used in this study were maintained in a specific pathogen-free facility of KAIST Laboratory Animal Resource Center. C57BL/6J mice aged 6–8 weeks were used in this study. After anesthetization with isoflurane, mice were transcardially washed with ice-cold 1× PBS supplemented with 10 U/mL heparin, followed by perfusion with ice-cold 4% PFA in 1× PBS. Mouse organs (brain, liver, small intestine, esophagus, stomach, kidney, lung, heart, and testis) were harvested and fixed in 4% PFA in 1× PBS at 4 °C for 2–6 h.

***In vivo* mitochondria labeling**. Experimental methods related to *in vivo* mitochondria labeling in mice were performed in accordance with protocols approved by the Korea Institute of Science and Technology Institutional Animal Care and Use Committee (KIST-IACUC). To label mitochondria in parvalbumin (PV)-positive neurons, Cre-dependent adeno-associated virus (AAV) expressing mScarlet followed by mitochondrial matrix-targeting sequence (from cytochrome C subunit VIII) was injected into PV-Cre mouse line (B6.129P2-Pvalb$^{\mathrm{tm1(cre)Arbr}}$/J), as follows. The mice were anesthetized with isoflurane and placed in a stereotaxic frame. 100 nL of 10:1 cocktail of AAV-Jx-synaptophysin-mVenus-T2A-mito-mScarlet was injected to subthalamic nucleus (STN, AP: +1.62 mm, ML: 1.65 mm, DV: -4.45, -4.55 and -4.65 mm) at a speed of 40 nL/min. Ten days after AAV injection, mice were transcardially perfused and the harvested brains were fixed with 4% PFA as mentioned above.

Mouse organ sample preparation. Fixed brains were sliced to a thickness of 150 µm with a vibratome (VT1000S; Leica, Wetzlar, Germany). Fixed organs were embedded in 4% (w/w) low gelling temperature agarose. The agarose was first melted and dissolved in deionized water with thermomixer (Thermomixer C model 5382; Eppendorf, Hamburg, Germany) at the temperature of 80 °C and then cooled to 40 °C. Organs were embedded in an agarose block by pouring the cooled agarose onto the fixed organs, oriented with a spatula, and then hardened at 4 °C for 1 h. Agarose block was then sliced to a thickness of 500–1000 µm with a vibratome. Agarose residue was then removed from the cut slices. Tissue slices were stored in 1× PBS containing 0.1 M glycine and 0.01% (w/w) sodium azide at 4 °C before use.

Zebrafish sample preparation. All the following procedures involving zebrafish larvae were approved either by the Korea Advanced Institute of Science and Technology Institutional Animal Care and Use Committee (KAIST-IACUC) or the Massachusetts Institute of Technology Committee on Animal Care and were in accordance with the National Institute of Health Guide for the Care and Use of Laboratory Animals. Wild-type, Casper (*mitfa*$^{w2/w2}$*; mpv17*$^{a9/a9}$), and *flk-egfp* (=*Tg*(*kdrl*:*EGFP*)) larval zebrafish (*Danio rerio*) aged 3–12 days-post-fertilization were used in this study. Larvae were first fixed with 4% PFA in 1× PBS at 4 °C for 6 h. Fixed specimens were then kept in 0.1% PBST (0.1% (w/w) Triton X-100 in 1× PBS) at 4 °C for 6 h for washing and permeabilization.

Fluorophore NHS-ester staining and expansion of mouse organs

i) Pre-gelation staining of mouse organs. Organ slices were permeabilized with 0.1% PBST (0.1% Triton X-100, 1× PBS) for 3 h. For pre-gelation staining of fluorophore NHS ester, organs were first stained with the diluted fluorophore NHS ester in 0.1% PBST for 6 h at 4 °C, followed by washing in 0.1% PBST three times for 30 min each time at RT. Next, 0.1 mg/mL 6-((acryloyl)amino)hexanoic acid (AcX) in 1× PBS was added with a concentration of 0.1 mg/mL for 6 h at RT. AcX-treated organ slices were washed in 1× PBS three times for 30 min each time at RT with gentle shaking. The slices were then subjected to gelation. The organ slices were first incubated with gelation solution (8.625% [w/w] sodium acrylate, 2.5% [w/w] acrylamide, 0.15% [w/w] *N,N'*-methylenebis(acrylamide) [BIS], 2 M NaCl, 0.2% [w/w] ammonium persulfate [APS], 0.2% [v/v] tetramethylethylenediamine [TEMED], 0.01% [w/w] 4-hydroxy-2,2,6,6-tetramethylpiperidin-1-oxyl [H-TEMPO], 1× PBS) at 4 °C twice for 30 min each time, followed by incubation at 37 °C for 2 h. Gelled organs were then homogenized with 8 U/mL proteinase K in digestion buffer (1 mM ethylenediaminetetraacetic acid [EDTA], 50 mM Tris-HCl [pH 8.0], 0.5% Triton X-100, 1 M NaCl) 3–4 times at 37 °C for 12 h each time then 2–3 times at 60 °C for 6 h each time. Complete digestion was confirmed when the digested organ-gel composite is isotropically expanded by approximately 1.5-fold without distortion on its surface.

ii) Inter-digestion staining of mouse organs. For inter-digestion staining of organs with the fluorophore NHS ester, permeabilized organ slices were first treated with AcX, as described above. Then, gelation of organs was performed, followed by a single round of digestion with proteinase K for 4–12 h at 37 °C. After then, gels were stained with diluted fluorophore NHS ester in 0.1% PBST for at least 6 h at 4 °C, followed by washing in 0.1% PBST three times at RT for 30 min each time. After staining, further digestion was performed as described above until complete digestion of gelled organ slices was achieved.

iii) Post-digestion staining of mouse organs. For post-digestion staining of organs with the fluorophore NHS ester, permeabilization, AcX treatment, gelation, and digestion were conducted as previously described. Fully digested gels were stained with diluted fluorophore NHS ester in 0.1% PBST for at least 6 h at 4 °C, followed by washing in 0.1% PBST three times at RT for 30 min each time.

iv) DAPI staining and expansion. For all three staining methods, fully digested, NHS-ester-labeled gels were stained with DAPI diluted in 1× PBS at 4 °C, then washed with 1× PBS three times for 30 min each time at 4 °C. After DAPI staining, the gels were washed with an excess volume of deionized water for expansion until the size of the gels plateaued. Detailed labeling methods and imaging conditions of the mouse organs are provided in **Supplementary Table 3**.

Primary antibody, secondary antibody, DNA-conjugated secondary antibody preparation. The following primary antibodies were used: goat anti-FITC Alexa Fluor 488, rabbit anti-Homer1, rabbit anti-SLC2A1, rabbit anti-RFP, mouse anti-Bassoon, chicken anti-GFP, chicken anti-GFAP, guinea pig anti-MAP2, and rat anti-MBP. The following fluorophore-conjugated secondary antibodies were used: goat anti-mouse CF 405S, goat anti-mouse Alexa Fluor 488, goat anti-mouse Alexa Fluor 546, goat anti-rat Alexa Fluor 488, goat anti-rabbit Alexa Fluor 488, goat anti-rabbit Alexa Fluor 546, goat anti-rabbit CF 633, and goat anti-chicken Alexa Fluor 546. DNA-conjugated secondary antibodies were used for sequential imaging. DNA-antibody conjugation was performed as previously described in iExM protocol[53]. Detailed information about the antibodies used in this study is provided in **Supplementary Table 2**; complete DNA sequences are presented in **Supplementary Table 4**.

Antibody co-staining with fluorophore NHS ester and expansion of the mouse brain. First, brain slices were blocked and permeabilized with normal goat serum (NGS) blocking buffer (5% [w/w] NGS, 0.2% [w/w] Triton X-100, 1× PBS) for 3 h. For brain slices that were imaged for actin, the permeabilized brains were stained with fluorescein phalloidin in 0.1% PBST overnight at 4 °C followed by washing in 0.1% PBST three times for 30 min each time. Brain slices were then incubated with primary antibodies in NGS blocking buffer for at least 6 h at 4 °C, followed by washing in 0.1% PBST three times for 30 min each time. Secondary antibodies diluted in NGS blocking buffer were then added for at least 6 h at 4 °C followed by washing in 0.1% PBST three times for 30 min each time. For pre-gelation staining with the fluorophore NHS-ester-, antibody-stained brains were treated with diluted fluorophore NHS ester in 0.1% PBST for at least 6 h at 4 °C, followed by washing in 0.1% PBST three times for 30 min each time. Then, 0.1 mg/mL AcX in 1× PBS was added for at least 6 h at 4 °C, followed by washing in 1× PBS three times for 30 min each time. Gelation and digestion of brains was then performed as previously described in proExM protocol[18]. For post-digestion staining of brain slices with the fluorophore NHS ester, digested gels were treated with diluted fluorophore NHS ester in 0.1% PBST for at least 6 h at 4 °C, followed by washing in

0.1% PBST three times for 30 min each time. The gels were then washed with an excess volume of deionized water for expansion until the size of the gel plateaued. Expanded specimens were stored in the dark at 4 °C before imaging.

Fluorophore NHS-ester staining and expansion of larval zebrafish

i) Gelation. ExM of larval Zebrafish was performed using the previously described proExM protocol[18] with several modifications. Fixed and permeabilized specimens were incubated in 0.1 mg/mL AcX in 0.1% PBST three times for 6 h each time at 4 °C, then washed with 0.1% PBST three times for 30 min each time at 4 °C. The specimens were then incubated with a gelation solution (8.625% [w/w] sodium acrylate, 2.5% [w/w] acrylamide, 0.15% [w/w] BIS, 0.2% [w/w] 2,2'-azobis[2-(2-imidazolin-2-yl)propane] dihydrochloride [VA-044], 0.05% [w/w] Triton X-100, 2 M NaCl, 1× PBS) three times for 6 h each time at 4 °C with gentle shaking. After incubation, each zebrafish was placed between two pieces of #1 cover glass filled with a freshly prepared gelation solution and incubated at 45 °C for 4 h in a humidified, nitrogen-filled chamber.

ii) Pre-digestion. After careful removal of the upper glasses, the cover glasses with attached hydrogels were rinsed with 0.1% PBST multiple times. Excess gel around the specimens was removed using a razor blade, and the resulting rectangle-shaped hydrogels were detached from the cover glasses with a wet paintbrush. The gels were then transferred into a 12-well plate for pre-digestion in 1.5 mL of pre-warmed digestion buffer (1 mM EDTA, 50 mM Tris-HCl [pH 8.0], 0.5% [w/w] Triton X-100, 1 M NaCl) supplemented with 16 U/mL proteinase K and incubated three times for 6–12 h each time at 37 °C with gentle shaking. Finally, gels were incubated in staining base buffer (0.1% Triton X-100, 1 M NaCl, 1× PBS) three times for 30 min each time at 4 °C for washing.

iii) Inter-digestion staining of fluorophore NHS ester. For NHS-ester staining of zebrafish, the NHS ester (Alexa Fluor 488 NHS ester, ATTO 647N NHS ester) stock solutions (10 mg/mL in anhydrous DMSO) were stored at -20 °C, then diluted to 1:1000 in cold staining base buffer to prepare the staining solution. Following pre-digestion, the gels were incubated with freshly prepared staining solution for at least 12 h at 4 °C with gentle shaking, then washed with staining base buffer three times for 30 min each time at 4 °C.

iv) Post-digestion and decalcification. For post-digestion, gels were treated with 16 U/mL proteinase K in digestion buffer at 37 °C, 8–12 times for 6 h each time. To completely remove calcium ions that may have been released from digested bone, cartilage, and calcified tissues, fully digested samples were treated with an excess volume of decalcification solution (10% [w/w] EDTA, 1 M NaCl, 1× PBS) three times for

30 min each time at RT with gentle shaking.

v) Expansion. Decalcified gels were serially washed with decreased concentrations of NaCl (1 M NaCl, 0.8 M NaCl, 0.6M NaCl, 0.4 M NaCl, 0.2 M NaCl) for 30 min each at RT. The gels were then washed with an excess volume of deionized water three times for at least 30 min each time at RT, and then kept in fresh deionized water overnight at 4 °C for full expansion. Expanded specimens were stored in the dark before imaging.

GFP imaging of whole zebrafish larvae. Transgenic *flk-egfp* zebrafish larvae at 3 dpf were dechorinated and then fixed with 4% PFA in 1× PBS for 1 h at 4 °C. After fixation, the larvae were washed three times with 0.1% PBST. In order to test endogenous GFP signal retention after proteinase digestion, the larvae were processed according to the previously described whole-ExM protocols with several modifications. Briefly, larvae were transferred into AcX solution, incubated for 6 h at 4 °C, then washed with 0.1% PBST three times for 30 min each time at 4 °C. After AcX treatment, larvae were incubated with pre-gel solution (8.625% [w/w] sodium acrylate, 2.5% [w/w] acrylamide, 0.15% [w/w] BIS, 0.2% [w/w] VA-044, 0.05% [w/w] Triton X-100, 2 M NaCl, 1× PBS) for 12 h at 4 °C, followed by polymerization for 4 h at 37 °C. Sample homogenization was performed using 16 U/mL proteinase K in a digestion buffer at 37 °C. After 54 h-long digestion, the specimens were washed with 0.1% PBST multiple times and imaged with a confocal microscope. In order to test whether the whole-ExM protocol is compatible with post-digestion antibody labeling against GFP, gelled larvae specimens were first digested for 36 h at 37 °C, incubated with freshly prepared NHS-ester staining solution for 12 h at 4 °C with gentle shaking, then washed with staining base buffer three times for 30 min each time at 4 °C. After NHS-ester staining, the specimens were further digested with proteinase K for 18 h at 37 °C, and washed with 0.1% PBST three times for 30 min each time at 4 °C. Specimens were then blocked with NGS blocking buffer for 2 h at 4 °C. Then, specimens were incubated with anti-GFP antibody in NGS blocking buffer for 24 h at 4 °C, followed by washing in NGS blocking buffer three times for 30 min each time at 4 °C. Secondary antibody diluted in NGS blocking buffer was then added for 12 h at 4 °C followed by washing in NGS blocking buffer three times for 30 min each time, and 0.1% PBST three times for 30 min each time. Specimens were then washed in deionized water for expansion and imaging.

ExFISH of whole zebrafish larvae. The zebrafish larvae were processed and expanded according to the proExM and ExFISH protocols[18,22,57]. Briefly, zebrafish larvae were fixed using 4% PFA in 1× PBS for 20 min at 4 °C. After fixation, the larvae were washed twice with Modified Barth's Saline (MBS) buffer at pH 6.0 and incubated overnight with 0.1 mg/mL of AcX in MBS buffer at RT. For ExFISH processing, incubation with AcX was followed by incubation with homemade LabelX in 3-(*N*-Morpholino)propanesulfonic acid (MOPS) buffer at pH 7.7, overnight at 37 °C. Zebrafish were transferred to StockX solution and incubated overnight at 4 °C. Before gelation, zebrafish were transferred into fresh StockX solution containing H-TEMPO, TEMED, and APS in 94:3:2:2 StockX:H-TEMPO:TEMED:APS, incubated for 1 h at 4 °C, and polymerized in gelation chamber for 2 h at 37 °C. Sample homogenization was performed using 8 U/mL proteinase K in a buffer containing 50 mM Tris-HCl (pH 8.0), 500 mM NaCl, 40 mM $CaCl_2$, for 10 h at 37 °C. For proExM, the gel was washed in deionized water for 3–4 times for 15 min each and expanded in deionized water for at least 6 h at RT. For ExFISH, gelled samples were processed as described before using HCR-initiator-tagged FISH probes hybridization for *SNAP-25* and *β-actin* followed by hybridization chain reaction amplification with HCR hairpin stocks labeled with Alexa Fluor 546 and Alexa Fluor 647 fluorophores. ExFISH processed samples were expanded in 0.05× saline sodium citrate (SSC).

Determination of expansion factor. The expansion factor for the mouse organs and zebrafish larvae was quantified by measuring the gel size before and after expansion. Concurrently, the same structural landmarks were imaged pre- and post-expansion, and the expansion factor was calculated from these landmarks. Expansion factor of the mouse organs are displayed in **Supplementary Fig 5**. For all zebrafish experiments in this study, the expansion factor determined by landmarks was approximately 4.1-fold, coincident with the expansion factor determined by gels.

Reproducibility. In this study, more than 50 zebrafish aged 3–12 dpf were used for protocol optimization and confirmation, and more than 20 zebrafish from this cohort were imaged for data acquisition. All images in **Figs. 2–4** and **Supplementary Figs. 22–32** were acquired from at least 5 independent experiments.

Sequential imaging

i) Immunostaining of brain tissue for sequential imaging. Brain slices were first blocked and permeabilized with normal donkey serum (NDS) blocking buffer (5% NDS, 0.2% Triton X-100, 1× PBS) for 2 h. Brain slices were then treated with 0.1 mg/mL AcX in 1× PBS, followed by washing in 1× PBS three times for 30 min each time. Then, brain slices were incubated with primary antibodies in NDS blocking buffer for 3 h, followed by washing in NDS blocking buffer four times for 30 min each time. Next, brain slices were incubated with DNA-conjugated secondary antibodies in hybridization buffer (5% NDS, 0.2% Triton X-100, 2× SSC, 0.2 mg/mL sheared salmon sperm DNA) overnight, followed by washing in NDS blocking buffer four times for 30 min each time. Brain slices were then incubated with 1 ng/µL DNAs with 5' acrydite modification (which we designated "tertiary DNAs") in hybridization buffer overnight then washed in NDS blocking buffer four times for 30 min each time.

ii) Gelation, expansion, and re-embedding of brain tissue for sequential imaging. Tertiary DNA-stained brain slices were incubated in pre-gel solution (8.625% [w/w] sodium acrylate, 2.5% [w/w] acrylamide, 0.2% [w/w] *N,N'*-(1,2-dihydroxyethylene) bisacrylamide [DHEBA], 1.865 M NaCl, 1× PBS) overnight at 4 °C with gentle shaking. After incubation, brain slices were incubated in gelation solution (8.625% [w/w] sodium acrylate, 2.5% [w/w] acrylamide, 0.2% [w/w] DHEBA, 1.865M NaCl, 1× PBS, 0.2% [w/w] APS, 0.2% [v/v] TEMED, 0.01% [w/w] H-TEMPO) twice at 4 °C for 30 min each time. Then, the slices were subjected to gelation and digestion as previously described in the iExM protocol[53]. Digested gels were then briefly rinsed with 0.1% PBST three times and stained with fluorophore NHS ester in 0.1% PBST overnight at 4 °C with gentle shaking. After staining, gels were washed with 0.1% PBST three times for 30 min each time. The gels were then washed with an excess volume of deionized water for expansion until the size of the gel plateaued. Expanded gels were then re-embedded as previously described in iExM protocol[53].

iii) Imager DNA hybridization and dehybridization of re-embedded brain slices for sequential imaging. Re-embedded gels were pre-hybridized in DNA hybridization buffer (4× SSC, 20% formamide) for 30 min. Pre-hybridized specimens were incubated with imager DNAs (**Supplementary Table 5**) at a concentration of 1.5–2 ng/µL in DNA hybridization buffer, and washed in DNA hybridization buffer six times for 1 h each time, followed by washing once in 1× PBS for 30 min. Washed gels were then incubated with DAPI diluted in 1× PBS for 1 h, washed with 1× PBS 2 times for 30 min each time, and then imaged. The imaged gels were treated with an excess volume of 50% formamide twice at 60 °C for 1 h each time to fully dehybridize the imager DNAs. Gels were then pre-hybridized in DNA hybridization buffer for the next round of imager DNA hybridization (**Supplementary Table 5**). Aforementioned procedures are repeated to acquire multiple rounds of sequential images.

iv) Two-dimensional image registration. After acquiring sequential images of re-embedded brains, 1st and 2nd round images were registered to the 3rd round image using the bUnwarpJ[58] plugin in Fiji. In detail, 1st and 2nd round fiducial marker images (either DAPI or Cy3) were registered to 3rd round fiducial marker image, and the respective transformation was saved. The saved transformation was then applied to 1st and 2nd round images obtained from structures labeled with Alexa Fluor 488- and ATTO 647N-conjugated imager DNAs, and merged with the 3rd round image to create hyperstack images of the individual channel.

v) Three-dimensional image registration using Cy3 NHS ester. The overall three-dimensional registration was performed in two steps: a coarse three-dimensional registration and a fine two-dimensional registration. For coarse three-dimensional registration, both the target image (i.e., fixed image) and the source image (i.e., moving image) along the lateral directions (i.e., x and y) were down-sampled by a factor of 64. Subsequently, we acquired the three-dimensional displacement field that aligned the reference channel (Cy3 NHS ester) of the source image with that of the target image. Because the displacement field was calculated for the down-sampled images, it was up-sampled along the lateral directions and scaled by a factor of 64 to make it applicable to the original source image. Coarse registration was then performed by applying the transformed displacement field to each channel of the source image. For fine two-dimensional registration, each pair of z-slices from the target image and the coarse-registered source image were registered in a slice-by-slice manner. The slices were down-sampled by a factor of four, and the two-dimensional displacement field was calculated using the reference channel. The displacement field was then up-sampled and scaled by a factor of four, then applied to each channel of the z-slice from the coarse-registered source image to obtain the fine registration result. All three-dimensional image registrations were performed using custom-written MATLAB codes.

Sample mounting and imaging. For the imaging of expanded hydrogels, the hydrogels were attached to 48 × 60 mm cover glasses to prevent hydrogel drifting during imaging. To ensure firm attachment, the cover glasses were treated for 30 min with 0.1% poly-L-lysine and then washed with deionized water. The hydrogels were then placed on cover glasses and immediately imaged by confocal microscopy. Specimens were imaged on a Nikon Eclipse T*i*2-E (Tokyo, Japan) microscope, with either a spinning disk confocal microscope (Dragonfly 200; Andor, Oxford Instruments, Abingdon, UK; CSU-XI; Yokogawa Electrical Corporation, Tokyo, Japan) equipped with a Zyla 4.2 sCMOS camera (Andor, Oxford Instruments) or a laser scanning confocal microscope (Nikon C2+, Nikon). Objectives used were 40× 1.15 NA water immersion lens, and 10× 0.45 NA air lens.

Data availability statement. The data that support the findings of this study are available from the corresponding author upon request.

REFERENCES

57. Asano, S. M. *et al.* Expansion Microscopy: Protocols for Imaging Proteins and RNA in Cells and Tissues. *Curr. Protoc. Cell Biol* **80**, e56. (2018). doi:10.1002/cpcb.56

58. Arganda-Carreras, I. *et al.* Consistent and elastic registration of histological sections using vector-spline regularization. in *Lecture Notes in Computer Science (including subseries Lecture Notes in Artificial Intelligence and Lecture Notes in Bioinformatics)* (2006). doi:10.1007/11889762_8

ACKNOWLEDGEMENTS

This work was supported by the Samsung Research Funding & Incubation Center for Future Technology (SRFC-IT1702-09). J.S.K. was supported by Samsung Scholarship. We acknowledge Prof. Taeyun Ku and Young Seo Kim for their helpful discussions. We acknowledge Su Yeon Kim and Dr. Jang Soo Yuk for their help with transgenic mouse experiments. We also acknowledge Yun-Mi Jeong and Hoi-Khoanh Giong for their help with zebrafish experiments.

AUTHOR CONTRIBUTIONS

J.S., C.E.P., I.C., K.M., J.-S.L., J.K., J.S.K., K.D.P., and E.E.J. performed the experiments and analysis. J.S. and J.-S.L. analyzed the anatomical structures of expanded larvae. Y.C. analyzed the anatomical structures of expanded mouse organs. J.K. and Y.-G.Y. performed three-dimensional registration. S.-K.K. prepared *in vivo* mitochondria-labeled mouse brain. All authors wrote the paper and contributed to the editing of the paper. E.S.B. and J.-B.C. supervised this work.

COMPETING FINANCIAL INTERESTS

J.-B.C., J.S., C.E.P., I.C., and K.M. have applied for a patent on whole-ExM (KR patent application 10-2021-0024480).